ELSEVIER

Tectonophysics 356 (2002) 307–322

TECTONOPHYSICS

www.elsevier.com/locate/tecto

Interaction of faults and perturbation of slip: influence of anisotropic stress states in the presence of fault friction and comparison between Wallace–Bott and 3D Distinct Element models

C. Pascal *

Laboratoire de Tectonophysique, UPMC, bte 129, 4, pl. Jussieu 75252, Paris cédex 05, France

Received 17 April 2001; accepted 1 August 2002

Abstract

Two decades after their birth, the validity of fault slip inversion methods is still strongly debated. These methods are based upon a very simplified mechanical background, the Wallace–Bott hypothesis. Following previous studies, the 3D Distinct Element Method (3DEC software) is used to explore the effect of varying stress anisotropy (i.e. the ''shape'' ratio) on slip perturbation along pairs of faults. Two end-member configurations are modelled in taking into account fault friction and internal deformation of faulted blocks. The first model deals with a relatively simple case where two nonintersecting conjugate normal faults are reactivated in an oblique normal stress regime. The second one simulates an extreme situation where two perpendicular intersecting faults are submitted to oblique extension. The average direction of fault slip predicted by 3DEC models is compared to the corresponding slip predicted by the simplified Wallace–Bott model. For the two simulated cases, it is shown that results from 3DEC and Wallace–Bott models are mutually consistent and argue for the validity of fault slip data inversion methods. Consistency remains even if slip is significantly deviated near the intersection line of faults. These deviations depend on the degree of anisotropy of applied stresses in presence of fault friction. Furthermore, modelling results suggest that, for intersecting faults with convergent slip directions, consideration of fault friction in the models leads to reduction of slip perturbation. In other words, modelling results lead to the nonintuitive conclusion that the validity of the simplified Wallace–Bott model is strengthened when 3DEC model's complexity (i.e. the number of parameters incorporated) increases.

Keywords: Microtectonics; Numerical modelling; Fault interaction; Fault slip data inversion

1. Introduction

Although their validity is still strongly debated (Twiss and Unruh, 1998; Gapais et al., 2000; Maerten, 2000), fault slip inversion methods (Carey and Brunier, 1974; Angelier, 1975; Gephart and Forsyth, 1984; Reches, 1987) are nowadays commonly accepted and used. The polemics arise from their background assumptions, the so-called Wallace–Bott hypothesis (Wallace, 1951; Bott, 1959). The Wallace–Bott hypothesis incorporates the following assumptions: (1) slip on fault surfaces occurs parallel to the greatest resolved shear stress, (2) faults are planar, (3) blocks are rigid, (4) neither stress perturbations nor block rotations along fault surfaces occur,

* Present address: Faculty of Earth Sciences, Vrije Universiteit, De Boelelaan 1085, 1081 HV Amsterdam, Netherlands. Fax: +31-20-646-2457.

E-mail address: pasc@geo.vu.nl (C. Pascal).

0040-1951/02/$ - see front matter © 2002 Elsevier Science B.V. All rights reserved.
PII: S0040-1951(02)00413-4

and (5) the applied stress state is uniform. These assumptions imply very drastic simplifications of the mechanical problem and seem to disagree with field observations, such as geometrical complexity of fault surfaces (e.g. Wallace and Morris, 1986; Tibaldi, 1998), local stress perturbations as evidenced by microstructures (Hancock, 1985; Petit, 1987) and block rotations along fault surfaces (Twiss and Geffel, 1990; Twiss et al., 1991; Pascal, 1998). Hence, one may wonder as to what extend these simplifications invalidate from the start the validity of inversion methods. Indeed, the use of fault slip data inversion methods in numerous field studies demonstrated that this is not the case (e.g. Mattauer and Mercier, 1980; Zoback et al., 1981; Angelier et al., 1985; Barrier and Angelier, 1986; Letouzey, 1986; Bergerat, 1987; Mercier et al., 1987; Huchon et al., 1991). One of the most convincing examples of such a demonstration was given by Le Pichon et al. (1988). The reconstructed Cenozoic paleostress patterns in the western European Platform (Bergerat, 1987) were found to be in good agreement with paleomagnetic studies and paleogeographic reconstructions (Le Pichon et al., 1988). Such a demonstration was empirical and a theoretical approach of the problem was still needed. Dupin et al. (1993) and Pollard et al. (1993) pioneered the use of numerical methods to check the validity of the Wallace–Bott hypothesis. Their preliminary results suggest that slip senses predicted by more refined mechanical models (i.e. including internal deformation of faulted blocks and interaction between faults) do not differ significantly from those predicted by the simplified Wallace–Bott model. More recently, Maerten (2000) explored numerically the consequences of varying geometry of intersecting faults on slip directions. He concluded that significant deviations to the Wallace–Bott model are expected close to the intersection line between faults. However, the complete set of degrees of freedom has not been explored yet. In particular, little attention has been paid until now on the influence of varying stress anisotropy on slip perturbation, in the presence of fault friction.

Following Dupin et al. (1993), the 3D Distinct Element Method (3DEC) was used to model various fault configurations of intersecting and nonintersecting pairs of faults. In order to reproduce very general cases, each model was submitted to polyaxial stress states with principal axes being significantly oblique to fault orientations. Two particular models are presented here. They represent two end-member cases where moderate and strong slip perturbations, respectively, can be expected. The first model deals with the relatively simple case of a conjugate pair of nonintersecting normal faults reactivated in an oblique normal stress regime (i.e. σ_3 oblique to fault strike). In the second model, two intersecting faults with perpendicular strikes are submitted to oblique extension. The average directions of slip on the fault planes are compared to the directions of slip predicted by the Wallace–Bott model. Finally, mechanical consistency of the models is discussed through consideration of the modelled strain patterns.

2. Modelling procedure

2.1. Principles of the 3D Distinct Element Method

The commercial software 3DEC (Itasca Consultants) is a 3D version of the Distinct Element Method (DEM, Cundall, 1971, 1988). The purpose of the numerical DEM is to calculate stress and strain inside discontinuous media such as fractured rock masses. Mechanical equations are time-integrated and solved using a finite differences technique. In the DEM, the medium is divided into several distinct blocks (Fig. 1). Classical continuum constitutive laws are applied for the interior of each block and relative displacements between blocks are calculated. Blocks interact at their contacts, where constitutive laws are defined. Mathematical principles are briefly summarised below. A complete mathematical description of the DEM is given by Cundall (1980, 1988) and Last and Harper (1990).

Block displacements are calculated from out-of-balance moment and forces applied to the centre of gravity of each block. Resultant forces include boundary forces applied to the edges of the block and, possibly, gravity if introduced by the user. Block acceleration, $\ddot{\vec{u}}(t)$, is related to resultant forces, $\vec{F}(t)$, by Newton's second law:

$$\ddot{\vec{u}} = \frac{\vec{F}(t)}{m}, \tag{1}$$

where m represents block mass and t, time.

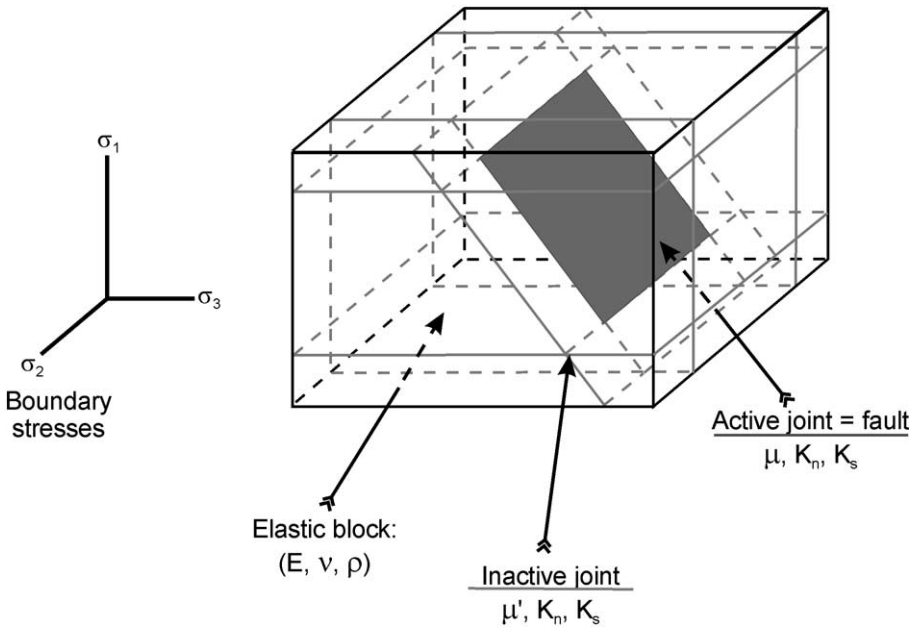

Fig. 1. Principle of the 3D Distinct Element Method. Active joints (i.e. faults) split elastic blocks apart. Blocks deform internally and are free to move along the faults when boundary stresses are applied. Inactive joints are used for technical purposes.

The new position of the block induces new conditions at block boundaries and thus new contact forces. The constitutive laws applied to the contacts are:

$$\Delta\sigma_n = k_n \Delta u_n, \tag{2}$$

$$\Delta\tau = k_s \Delta u_s, \tag{3}$$

where k_n, k_s are the normal and shear stiffness per unit area of the contact, $\Delta\sigma_n$, $\Delta\tau$ and Δu_n, Δu_s are the normal and shear stress increments and the normal and shear displacement increments, respectively. Stresses calculated at nodes located along contacts are submitted to the selected yield criterion (e.g. Mohr–Coulomb criterion):

$$\tau = \mu\sigma_n + c_0, \tag{4}$$

where μ is the coefficient of friction and c_0, cohesion. In order to prevent opening of the contacts, no tension is permitted along them:

$$\sigma_n \geq 0. \tag{5}$$

Internal deformation of blocks is taken into account in meshing the blocks into tetrahedra. Newton's second law is then applied at each node to calculate velocities and displacements. Strains are determined from displacements and stresses are derived from the constitutive law selected by the user. Pure elastic conditions as defined by Hooke's Law were applied for this study.

2.2. Parameters and modelling strategy

Two types of discontinuities are introduced into 3DEC models: active joints and inactive joints (Fig. 1). Active joints simulate faults. I considered here cohesionless faults with a coefficient of friction equal to 0.58 (i.e. corresponding to an angle of friction $\phi = 30°$). Cohesionless faults are assumed to exist at relatively shallow depths (Byerlee, 1978). Inactive joints were used to isolate active ones from the model boundaries and thus to prevent free surface effects. Their mechanical properties (Table 1) were selected in order to prevent block displacements along them. Following Dupin et al. (1993), a value of 200 GPa/m is adopted for both normal and shear stiffness per unit area of contacts. This value was empirically determined and prevents the contacts undergoing unrealistically drastic deformations. Elastic parameters and

Table 1
Parameters used in the modelling

Blocks rheology	
Young modulus	$E = 22$ GPa
Poisson's ratio	$\nu = 0.3$
Density	$\rho = 2300$ kg/m^3
Fault properties	
Coefficient of friction	$\mu = 0.58$
Cohesion	$C_0 = 0$
Normal and shear stiffness	$k_n = k_s = 200$ GPa/m
Properties of inactive joints	
Coefficient of friction	$\mu = 100$
Cohesion	$C_0 = 10^6$ GPa
Normal and shear stiffness	$k_n = k_s = 200$ GPa/m
Boundary stresses	
Initial confining pressure	5 MPa
Differential stress	$\Delta\sigma = 6$ MPa
	($\sigma_1 = 5$ MPa, $\sigma_3 = -1$ MPa)

density (Table 1) correspond to those measured in sedimentary rocks (e.g. Carmichael, 1989). An initial confining pressure of 5 MPa (i.e. representative of shallow depths in the upper brittle crust, Brown and Hoek, 1978) was set before application of boundary stresses. Extension was simulated as an initial stress relaxation along σ_2 and σ_3 axes, both axes being horizontal. The scale of the model was assumed to be small enough (i.e. $\sim$ 10 m) to be able to ignore the effects of the natural pressure gradient with depth. Models were carried out as a function of the "shape ratio" $\Phi=(\sigma_2-\sigma_3)/(\sigma_1-\sigma_3)$, with $0 \le \Phi \le 1$ (Angelier, 1975). For this study, Φ values were restricted to $0 < \Phi < 1$ in order to simulate the polyaxial stress states (i.e. $\sigma_1 \neq \sigma_2 \neq \sigma_3$) most likely to dominate in nature. The ratio Φ represents the geometry of the shape of the stress ellipsoid; hence, it represents one aspect of the anisotropy of the applied stress state. Practically speaking, models were carried out as a function of σ_2, keeping constant σ_1 and σ_3. The average direction of slip was calculated on each fault plane and compared to the sense of slip predicted by the Wallace–Bott model. The analytical SORTAN method (Pascal and Gabrielsen, 2001) was used to calculate Wallace–Bott slip on fault planes.

Finally, in order to track significant mismatches between applied boundary stresses (i.e. far-field stresses) and simulated stress fields in the faults' neighbourhood (i.e. perturbed local stress fields), the Mohr–Coulomb criterion was written as a function of the adopted degree of freedom, the ratio Φ (see Appendix A). For every fault plane of the following 3DEC experiments, the Mohr–Coulomb criterion is computed as a function of the ratio Φ applied at model boundaries. If fault reactivation is predicted for contrasting Φ values by 3DEC and by Eq. (18) (Appendix A), respectively, it means that the shear stress on the fault plane has been modified, with respect to the shear stress that would result form direct application on the fault of the boundary stresses. In other words, the local stress state is perturbed by kinematic interaction between faults. Note that it does not automatically imply that only the local Φ ratio is modified with respect to Φ applied. Local rotations of stress axes

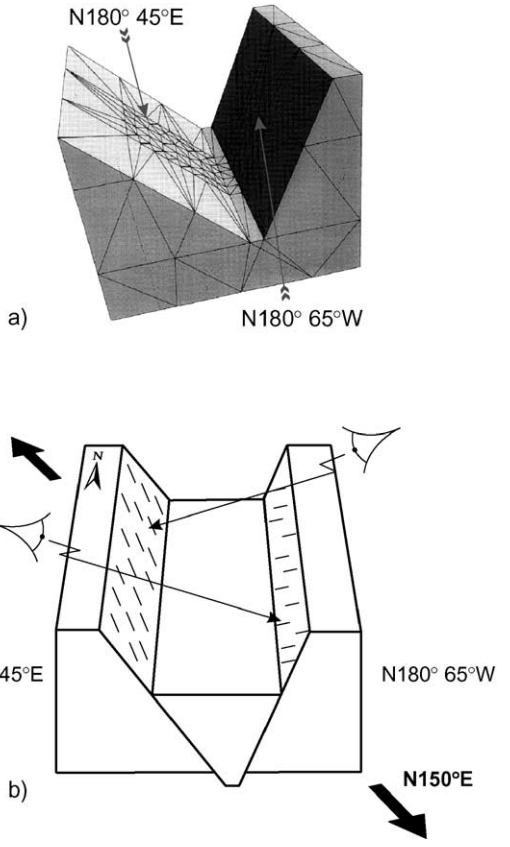

Fig. 2. 3DEC model 1. A pair of conjugate normal faults submitted to oblique extension. (a) 3DEC model. (b) Model sketch, note that fault displacements are magnified by 1000 times.

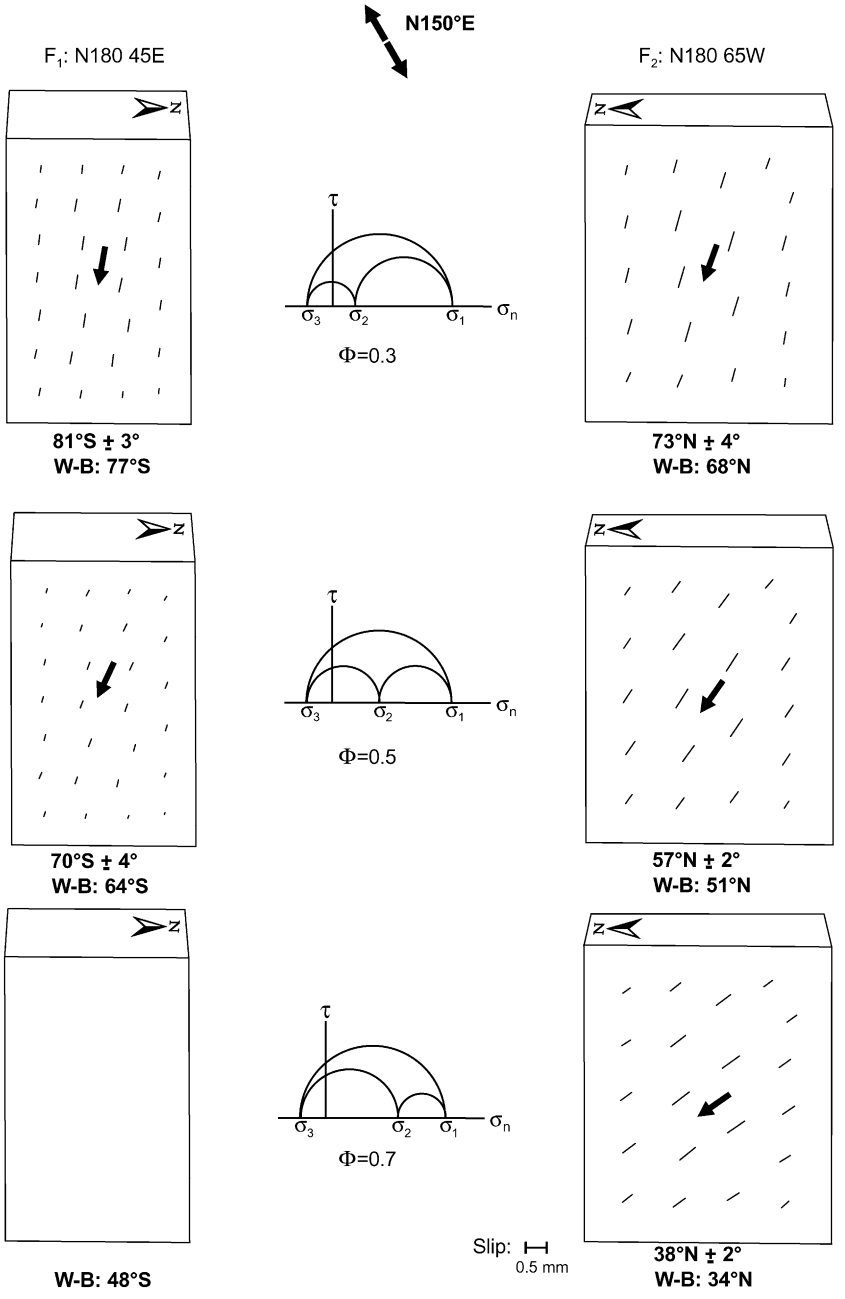

Fig. 3. Results of 3DEC model 1. Bars and arrows depict the local and average directions of slip on the two considered fault planes, respectively. Models are run as a function of the shape ratio Φ. The mean pitch of the slip vector and its associated standard deviation predicted by 3DEC is indicated. The pitch predicted by the Wallace–Bott (W–B) model is also shown.

can also explain the mismatch between 3DEC and Eq. (18) predictions.

3. Model 1: conjugate normal faults submitted to oblique extension

This first modelling attempt considers two conjugate normal faults reactivated in a normal stress regime with σ_3 horizontal and oblique to the dip direction of the faults (i.e. 60°, Fig. 2). Three different runs were performed, varying the "shape ratio" Φ (Fig. 3). The corresponding anisotropies of the applied stress field are presented as Mohr circles in Fig. 3. The three cases represent polyaxial stress states with $\sigma_1 \neq \sigma_2 \neq \sigma_3$: $\Phi = 0.3$ (i.e. σ_2 closer to σ_3 than to σ_1), $\Phi = 0.5$, (i.e. σ_2 equal to the mean value between σ_1 and σ_3) and $\Phi = 0.7$ (σ_2 closer to σ_1 than to σ_3). Arrows and bars on fault surfaces (Fig. 3) show the trace of the slip vector of the hanging wall and the local directions of slip, respectively. The mean pitch of the slip vector and its associated standard deviation were calculated for every fault plane at every run.

The first remark that can be made is that motion on fault F_1 stops when Φ reaches the value 0.7 (Fig. 3). More precisely, the 3DEC model predicts cessation of slip along F_1 for an applied Φ value falling between 0.5 and 0.7. Slip along F_2 occurs regardless of Φ. For comparison, the analysis presented in Appendix A is applied to the faults F_1 and F_2, when submitted to similar boundary stresses, and results are plotted as a function of Φ (Fig. 4). The Mohr–Coulomb criterion always predicts slip for F_2 independently of Φ and cessation of slip for F_1 when Φ exceeds the value 0.625 (Fig. 4b). A good correspondence was found between

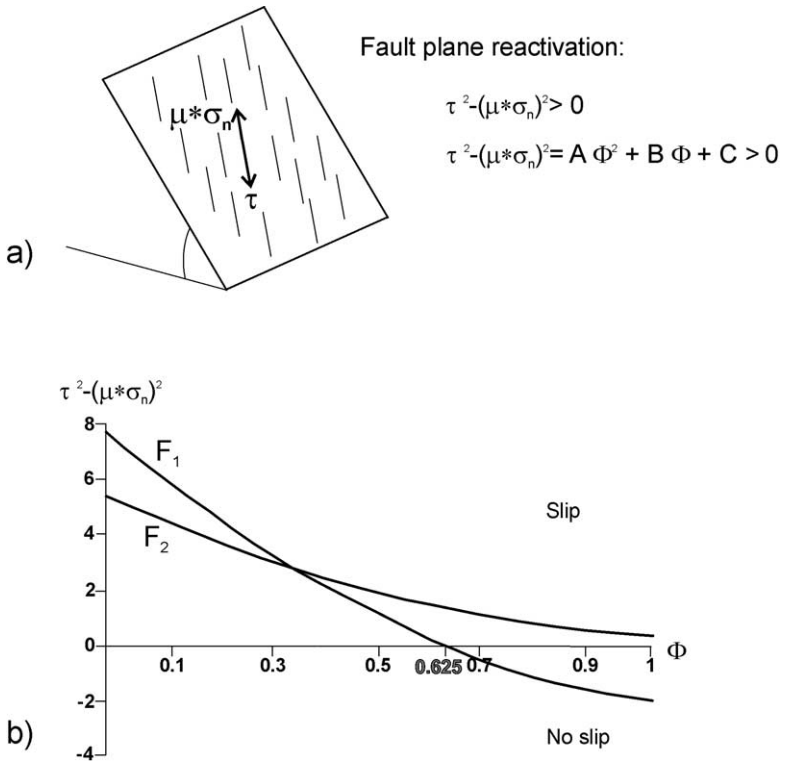

Fig. 4. Method used to track eventual local stress perturbations. (a) The Mohr–Coulomb criterion is written as a function of the shape ratio Φ. (b) Obtained parabolic functions are drawn for the two considered faults F_1 and F_2 in model 1. The predicted Φ value for cessation of slip along F_1 is compared with 3DEC results (Fig. 3). If consistent Φ values are found between analytical and 3DEC calculations, then the stress field is not significantly perturbed by fault interactions.

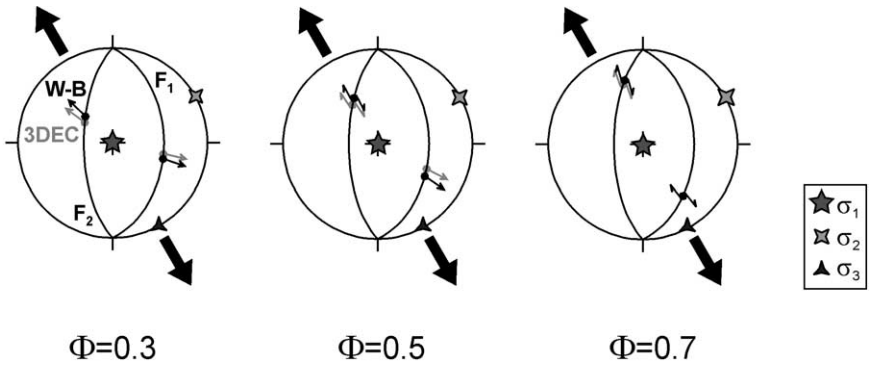

Fig. 5. Comparison between 3DEC and Wallace–Bott results for model 1. Applied principal stress axes are represented. Schmidt projection on the lower hemisphere.

3DEC results and analytical results derived from Eq. (18). In other words, for this specific fault and stress configuration, 3DEC predicts no significant perturbation of the magnitude of the resolved shear stress on fault planes.

A close inspection of the simulated slip directions on fault surfaces (Fig. 3) reveals that, when predicted for one given experiment (i.e. for $\Phi = 0.3$, 0.5 or 0.7), the directions of slip on one fault surface (i.e. F_1 or F_2) remain remarkably consistent. The standard deviation associated with the predicted mean pitch falls between 2° and 4°. The strongest deviations to the average motion are generally observed at the base of the fault surfaces (i.e. where accommodation space problems occur).

As expected from Wallace–Bott methods, motions become more oblique when the ratio Φ increases (Wallace, 1951). Comparison between the mean pitch predicted by 3DEC, for every fault at every run, and the corresponding Wallace–Bott pitch reveals that the mismatch between both models remains very modest (Figs. 3 and 5). Results from both models differ less than 6° for the two faults and the three runs.

4. Model 2: a pair of perpendicular intersecting faults submitted to oblique extension

The second model deals with a more complex fault pattern, where strong interactions between faults are expected. Model 2 involves a pair of perpendicular intersecting faults with σ_3 making angles of 30° and 60° with F_1 and F_2, respectively (Fig. 6). Results are presented as a function of Φ in Fig. 7, in using similar conventions as for Fig. 3.

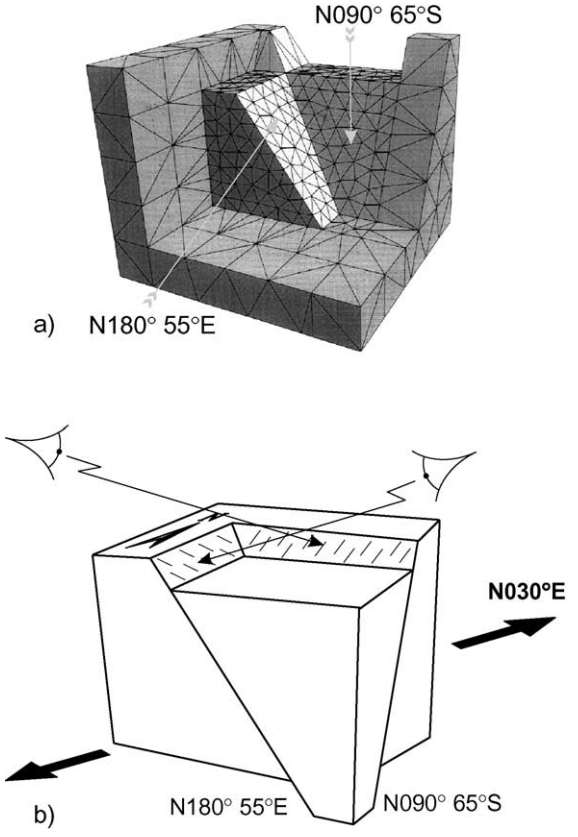

Fig. 6. 3DEC model 2. A pair of perpendicular and intersecting faults submitted to oblique extension. (a) 3DEC model. (b) Model sketch, note that fault displacements are magnified by 1000 times.

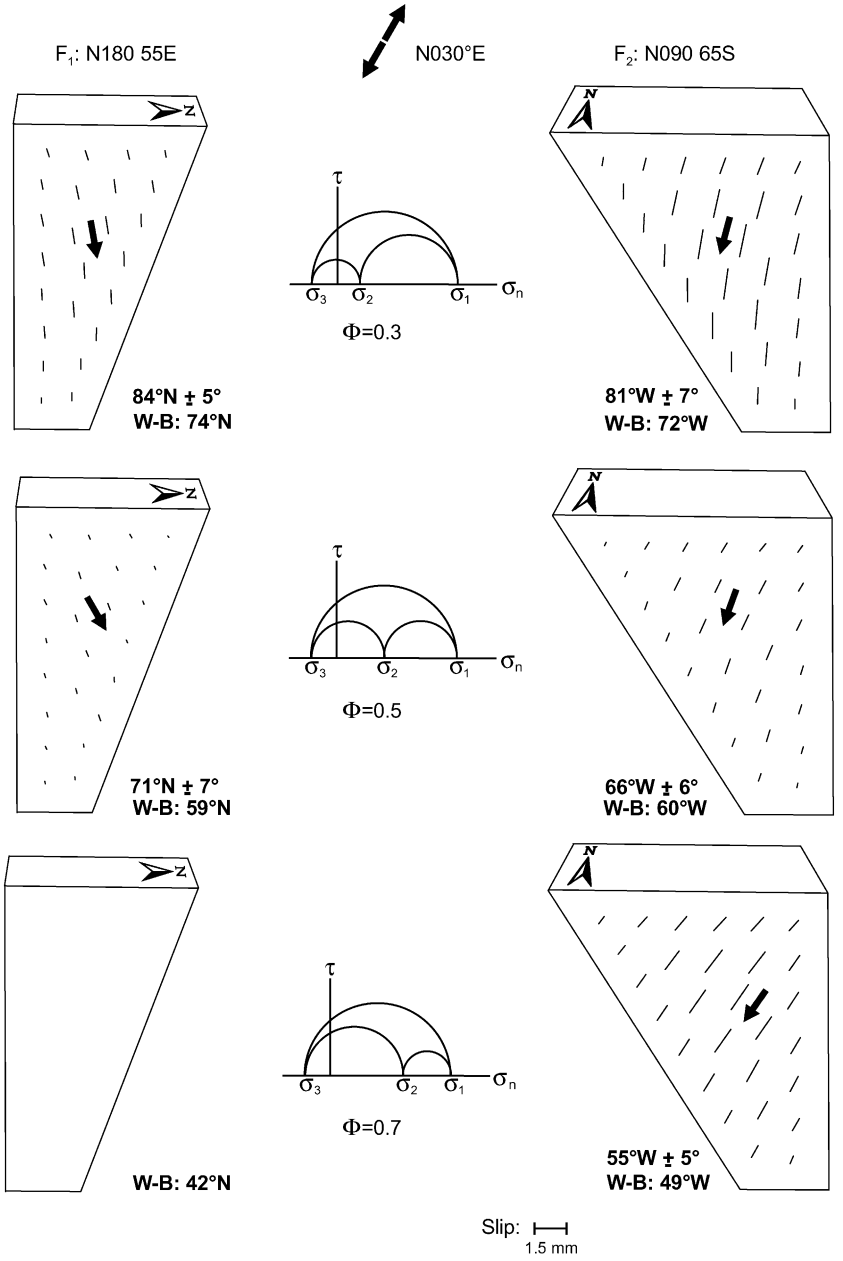

Fig. 7. Results of 3DEC model 2. Bars and arrows depict the local and average directions of slip on the two considered fault planes, respectively. Models are run as a function of the shape ratio Φ. The mean pitch of the slip vector and its associated standard deviation predicted by 3DEC is indicated. The pitch predicted by the Wallace–Bott (W–B) model is also shown.

Again the 3DEC model shows cessation of F_1 slip for applied shape ratio values falling between $\Phi = 0.5$ and $\Phi = 0.7$ (Fig. 7). However, when applied to the modelled faults, the analysis presented in Appendix A predicts reactivation for F_2 independently of Φ and no slip for F_1 when Φ overcomes the value 0.89 (Fig. 8). Hence, local stress fields promoting fault reactivation in the 3DEC model are significantly perturbed with

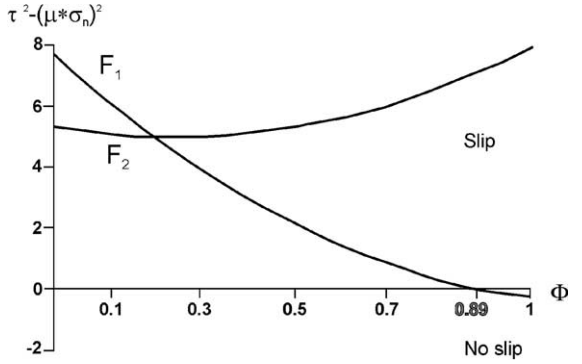

Fig. 8. The Mohr–Coulomb criterion written as a function of the shape ratio Φ. The predicted Φ value for cessation of slip along F_1 disagrees with 3DEC results from model 2 (see text and Fig. 7). Hence, the local stress field is significantly perturbed by fault interactions.

respect to applied boundary ones. Stress perturbation results in decreasing the efficiency of local stresses to reactivate fault F_1 (i.e. through decreasing the magnitude of the shear stress vector applied to F_1).

Consideration of directions of slip on fault surfaces (Fig. 7) shows that stress perturbation implies also perturbation of slip directions. Hanging-wall rotations are observed (e.g. Fig. 7, F_2 and $\Phi = 0.3$). As a consequence, the standard deviation of the calculated mean pitch is larger than in the previous model and reaches values between 5° and 7°. Slip is strongly perturbed close to the intersection line of the two faults. Perturbation operates in a way that slip tends to parallel this line as observed by Maerten (2000). For the two modelled faults, maximum block rotations (i.e. slip perturbation) are predicted for $\Phi = 0.3$ and rotations decrease with Φ. This effect is particularly highlighted by the decrease with Φ of the standard deviation related to the mean pitch of the slip vector on fault F_2. Interestingly, the amount of slip along F_1 also decreases with Φ. Furthermore, when faulting along F_1 is stopped (i.e. for $\Phi = 0.7$), slip rotations along F_2 become negligible. Hence, most of the slip perturbation is accounted by kinematic interactions between faults. In contrast, the standard deviation related to the mean pitch of the slip vector on fault F_1 increases between $\Phi = 0.3$ and $\Phi = 0.5$. However, it is worth noting that the predicted amount of slip on F_1 is drastically reduced when $\Phi = 0.5$. Thus, the apparent standard deviation increase for F_1 is more likely accounted the increase of systematic errors in calculating the mean pitch of the slip vector.

Comparison between predicted Wallace–Bott pitches and calculated 3DEC mean pitch on faults F_1 and F_2 is presented on stereoplots in Fig. 9. Despite the perturbations observed on particular regions of the fault planes, average block displacements and slip directions predicted by 3DEC and Wallace–Bott methods, respectively, remain in good agreement. The scatter between the results given by the two methods is in general less than 10° and equal to 12° for F_1 and $\Phi = 0.5$. As it is emphasised above, the results for this specific case are likely to be affected by errors. Nevertheless, it is remarkable that Wallace–Bott and 3DEC results converge for fault F_2 when Φ increases (Fig. 9). Hence, the amount of slip on fault F_1 decreases (Fig. 7). In other words, perturbations induced by F_1 on F_2 slip decrease with Φ. It implies that the scatter between

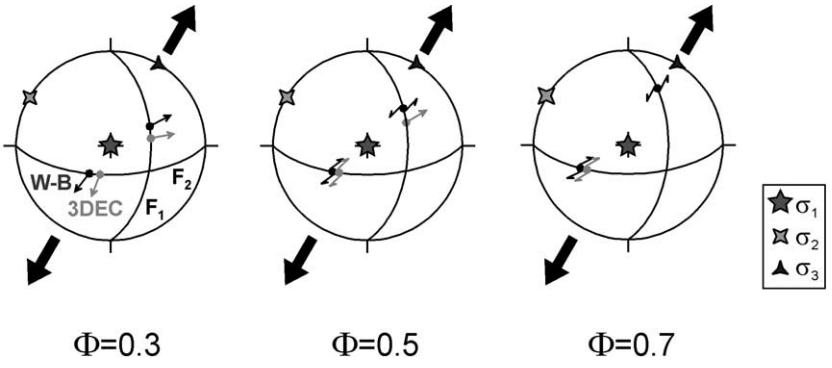

Fig. 9. Comparison between 3DEC and Wallace–Bott results for model 2. Applied principal stress axes are represented. Schmidt projection on the lower hemisphere.

3DEC and Wallace–Bott pitches calculated for F_2 decreases also with Φ and reaches a minimum value of 6° when F_1 slip becomes negligible (i.e. Fig. 7, $\Phi = 0.5$). Again, the relative disagreement between Wallace–Bott and 3DEC models is enhanced by local stress perturbations induced by fault interactions but remains relatively modest.

5. Discussion

5.1. Do modelled deformations remain realistic?

In order to check the ability of the present modelling approach to reproduce natural deformation, compatibility between bulk strain and strain induced by faulting deserves discussion. Some mechanical background assumptions, shared both by the Distinct Element Method (used by Dupin et al. (1993) and here) and the Boundary Element Method (used by Pollard et al., 1993; Maerten, 2000), may imply unrealistic solutions when modelling fault slip. Among these mechanical assumptions, the one that requires contacts to remain permanently closed (see Eq. (5)) is the more suspicious, because dilatation as a means of overcoming eventual strain compatibility problems is not permitted.

Dupin et al. (1994) showed that strains remain compatible in their 3DEC models when one single fault is considered. No strain compatibility problems are expected in the case of nonintersecting faults (i.e. model 1), because faults behave as they were isolated, as it is shown by the good agreement found between results from model 1 and those derived from simplified analytical solutions that neglect interactions between faults (i.e. Mohr–Coulomb criterion and the Wallace–Bott model, Figs. 3–5).

Strain compatibility problems, in the case of intersecting faults (i.e. model 2), have never been discussed previously, and interactions between fault planes may result in unrealistic strain distributions. According to applied boundary stresses and selected material properties (Table 1), the bulk strain (i.e. the volumetric strain) expected in the present models is $\sim 10^{-4}$. Fig. 10 shows strain distributions along horizontal sections of model 2 for the case $\Phi = 0.3$ (i.e. the case where maximum fault interaction is modelled). Predicted maximum strains are in the order of 10^{-4} along Y and Z axes (i.e. parallel to applied σ_3 and σ_1 axes, respectively), and thus remain consistent with applied boundary stresses and selected material properties.

The maximum slip predicted for the central parts of the modelled faults is in the order of a few mm and decreases gradually to reach zero at their edges (Figs. 3 and 7). Typical dimensions in the model (i.e. fault and block dimensions) are in the order of 10 m. Therefore, the magnitude of strain induced by the modelled faults is $\varepsilon \sim 10^{-3}/10 = 10^{-4}$. Results in Fig. 10 confirm that strain variations, induced by slip along faults, remain mechanically compatible with predicted slip increments and thus are in the same order than bulk strains. Note that (1) slip increments on natural microfaults in the range of mm to cm are common and (2) low strain values (i.e. $< 10^{-2}$) are in perfect agreement with strains associated to microfaulting (Carey, 1976).

To summarize, despite the background assumptions that are adopted, mechanical compatibility of the whole system is ensured by the numerical approach used here (i.e. the Distinct Element Method). Because results shown by Pollard et al. (1993) and Maerten (2000) remain consistent with those shown by Dupin et al. (1993) and here, mechanical compatibility is certainly ensured by the Boundary Element Method as well. In particular, the assumption of keeping closed contacts between blocks does not result in unrealistic strain patterns in the present case. Moreover, this assumption is obviously consistent with the use of fault inversion methods in the field. These Wallace–Bott methods require faults to remain closed during slip, in order to generate observable friction structures on their surfaces (i.e. slickenside lineations). However, it is worth noting that some observed kinematic indicators (e.g. growth-fiber slickenlines) imply dilatation on the fault plane.

Looking in more detail the modelled strain patterns, we see that the effect of slip in the models is to increase or decrease strain in faulted blocks close to the fault surfaces, and particularly close to terminations of faults (Fig. 10). Strain variations occur in response to build-up of released and restrained volumes at faults' terminations. The locations of released and restrained volumes are directly dependent on slip directions (e.g. Petit, 1987). This effect is shown in Fig. 10 for ε_y and ε_z. For example, the model is in bulk extension along Y (i.e. $\varepsilon_y > 0$, Fig. 10) and faults F_1 and F_2 display sinistral and dextral strike-slip components, respectively.

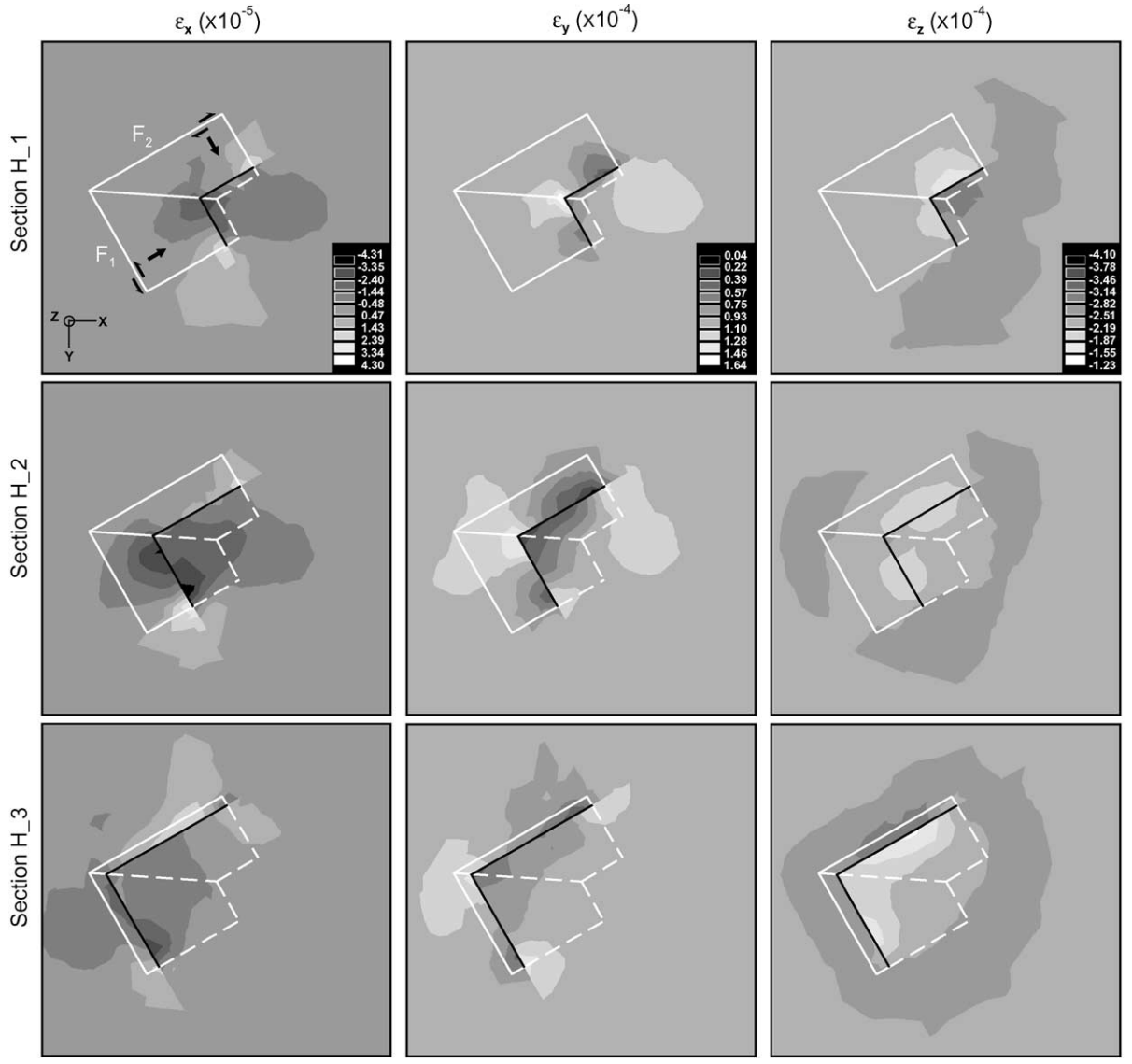

Fig. 10. Strain patterns predicted by 3DEC model 2, $\Phi = 0.3$. Horizontal sections H_1, H_2, and H_3 cut near faults' bottom, the middle of the model and near fault's top, respectively. Black lines represent intersections between sections and fault planes. Shortening is negative and lengthening positive. Note that X, Y and Z axes are parallel to σ_2, σ_3 and σ_1, respectively. See also Discussion for further explanation.

Therefore, tension is enhanced, or ε_y increases, in released volumes (i.e. Fig. 10: white and light grey areas). Similarly, tension is reduced, or ε_y decreases, in restrained volumes (i.e. Fig. 10: black and dark grey areas).

Due to the selected boundary conditions and material properties, strain along X is close to 0. Small variations of ε_x in the order of 10^{-5} occur close to the faults (Fig. 10). The present strain pattern suggests that minor compression of the downthrown block occurs parallel to X (Fig. 10: black and dark grey areas inside faults' acute angle). This effect remains consistent with the modelled slip directions (Fig. 7). Deformation of fault planes (i.e. minor bending of the faults towards the centre of the downthrown block) might explain why compression and extension also occur in a

symmetrical position relatively to the intersection line of faults and at faults' ends outside the acute angle, respectively (Fig. 10). However, this probable effect needs further exploration. Because ε_x reaches maximum values $\sim 10^{-5}$, it cannot be ruled out that numerical artefacts affect its associated distribution. Note that ε_x is 10 times less than the modelled bulk strain, therefore ε_x variations do not affect significantly the overall results of the modelling. Thus, not only the strain magnitudes are consistent in the models but also strain distributions are in good agreement with modelled fault kinematics.

It has been suggested (Reches, 1978, 1983) that general 3D strains cannot be accommodated by only two faults. This result seems to be contradicted by the results from the present study and previous ones (i.e. Dupin et al., 1993; Pollard et al., 1993; Maerten, 2000), which consider pairs of faults submitted to 3D deformation.

Reches (1978) assumes that rock masses include preexisting fault planes that are uniformly distributed in all directions of the 3D space (which in most cases seems to be geologically incorrect, e.g. Ramberg et al., 1977) and that strain can only be accommodated by slip on them. Internal deformation of faulted blocks is simply ignored. Thus, it is not surprising that such a model requires reactivation of various faults (generally more than two), regardless of strain magnitude, if no other mechanisms to accommodate 3D strains are allowed.

In the present models, pairs of preexisting fault planes were considered and faulted blocks were allowed to deform internally. Fig. 10 shows that 3D strains are accommodated both by faulting and elastic deformation of blocks. As pointed out above, strains remain compatible throughout the modelled volumes. Hence, it is shown here that a couple of faults is able to accommodate 3D strains when strain accommodation is assisted by internal deformation of faulted blocks. However, it is important to note that this mechanism is possible here, because strain associated to microfaulting is low. For low strain values, rocks behave as elastic bodies (e.g. Jaeger and Cook, 1979). If strain exceeds $\sim 10^{-2}$, nucleation of new faults and accommodation of strain by slip along them can be expected. This latter case is reasonably accounted by Reches and Dieterich's (1983) theory, but does not comply with microfaulting conditions.

5.2. Why and to what extend is the Wallace–Bott hypothesis valid?

Similar analyses from Dupin et al. (1993) and Pollard et al. (1993) already suggested that even taking into account the rheology of faulted blocks, slip discrepancies between numerical models and Wallace–Bott analytical model remain modest. Present models emphasise the effect of varying stress anisotropy in presence of fault friction. In case of no contact between faults, model 1 (Fig. 2) confirms the intuitive feeling that stress anisotropy (i.e. the Φ ratio) has no effect on slip perturbation. Slip directions can be predicted by the simplified Wallace–Bott model (Fig. 5).

Model 2 (Fig. 6) suggests that, when faults intersect and display convergent motions, stress anisotropy is a key parameter in controlling fault interaction and, consequently, in controlling slip perturbation (Fig. 7). In the present case, intersection between faults inhibits the ability of one of the faults to be reactivated for a given stress state (i.e. comparison of results from Figs. 7 and 8 shows that slip along F_1 stops for lower Φ values than predicted by the Mohr–Coulomb criterion if the fault would be driven directly by boundary stresses). More precisely, the progressive increase, as a function of Φ, of strike-slip along one fault of the intersecting system (i.e. F_2, Figs. 7 and 9) results in increasing normal pressure on the other fault surface. In turn, increasing normal pressure (i.e. decreasing the ratio τ/σ_n with respect to the coefficient of friction, see Eq. (4) with cohesion set to zero) on the latter fault results in decreasing slip along it (i.e. F_1, Fig. 7). Note that the fault of the intersecting system that "dominates" is the one that, because of its orientation in the 3D space with respect to the stress axes and the second fault plane, presents the best alignment between its average slip direction and the normal vector of the other fault plane. In the specific case of model 2, the dominant fault is the steepest one that also presents the most pronounced strike-slip between the two faults (i.e. F_2, Figs. 6 and 7).

Finally, slip decrease along the subordinate fault of the intersecting system, in function of the degree of anisotropy of the stress state, implies decrease of slip perturbation along the dominant fault. Hence, for the present modelled configuration, the mismatch between slip directions predicted by the 3DEC and

Wallace–Bott models reduces for the dominant fault (i.e. F_2, Fig. 9), as a function of Φ. This behaviour is particularly well depicted by the decrease, as a function of Φ, of hanging-wall rotation along F_2 (Fig. 7). Note that, because slip along the dominant fault is almost constant (Fig. 7, F_2), slip perturbation on the subordinate fault remains constant until slip stops (Fig. 9, F_1).

In summary, model 2 suggests that for extensional cases, where intersecting faults present convergent fault slip directions and friction is considered, slip perturbation reduces for one of the faults as a function of the ratio Φ. The complete set of possible configurations is however still to be explored. In particular, it is expected that, if intersecting faults present divergent fault slip directions, discrepancies between 3DEC and Wallace–Bott directions of slip will increase with Φ. Further work is needed in order to quantify these expected discrepancies.

Intersecting fault models carried out by Maerten (2000) neglected friction on faults. Consequently, the mechanism of slip decrease on one fault and reduction of slip perturbation along the other one, which is evidenced here, was not accounted for by these previous models. The present study agrees with Maerten's overall results that slip is significantly perturbed close to fault intersections, but it suggests that, in general, perturbation has been overestimated in his models.

6. Summary

Slip directions for two cases of intersecting and nonintersecting pairs of microfaults have been modelled using the numerical 3D Distinct Element Method. The models assumed internal deformation of blocks and fault friction. The degree of anistropy of the applied stress state (i.e. the Φ ratio) was taken as variable in the models and average slip directions were compared to slip directions predicted by the simplified Wallace–Bott model.

Both the simple model, addressing the case of a conjugate fault pattern, and the complex one, involving intersecting perpendicular faults, argue in favour of the validity of the simplified Wallace–Bott model, and hence in favour of the validity of fault slip data inversion methods. This result agrees both with field studies, which empirically showed the validity of these methods, and with previous numerical studies. In addition, modelling results suggest that, for intersecting faults with convergent slip directions, consideration of fault friction in the models leads to reduction of slip perturbation. That is to say, modelling results lead to the nonintuitive conclusion that the validity of the simplified Wallace–Bott model can be strengthened when 3DEC model complexities (i.e. the number of parameters accounted by) increase.

Acknowledgements

I am grateful to two anonymous reviewers for their constructive comments that helped to improve significantly the manuscript. This study is part of the author's PhD thesis granted by the French Ministry of Research and carried out in the framework of the project Elf Norge-University of Bergen-U.P.M.C. Claude "Pépé" Lepvrier and Jacques Angelier are acknowledged for supervising my PhD thesis and Dr. R. Seland and Dr. O. Minsaas for financial support and great interest in this work. Paul Reemst and Roy H. Gabrielsen participated to create a friendly atmosphere during the project. Special thanks to Jyr-Ching Hu for his help in guiding my first steps as 3DEC user. Dr. D. Billaux and Itasca France are acknowledged for flexibility during the renting periods of the software.

Appendix A

Consider a normal stress regime (i.e. σ_1 vertical) applied to one given fault plane. σ_3 strike is referenced by $\theta \in [0°;360°]$ (Fig. 11a). As usual, in Earth Sciences, $\sigma_3 \leq \sigma_2 \leq \sigma_1$ and compression is positive. The geometry of the fault plane is described by its dip direction (fault azimuth), $d \in [0°;360°]$, and its dip, $p \in [0°;90°]$ (Fig. 11b).

The normal and shear stress applied to the fault plane are (e.g. Angelier, 1994):

$$\boldsymbol{\sigma}_{\mathbf{n}} = ((T\mathbf{n}) \cdot \mathbf{n}) \cdot \mathbf{n}, \tag{6}$$

$$\boldsymbol{\tau} = T\mathbf{n} - \boldsymbol{\sigma}_{\mathbf{n}}, \tag{7}$$

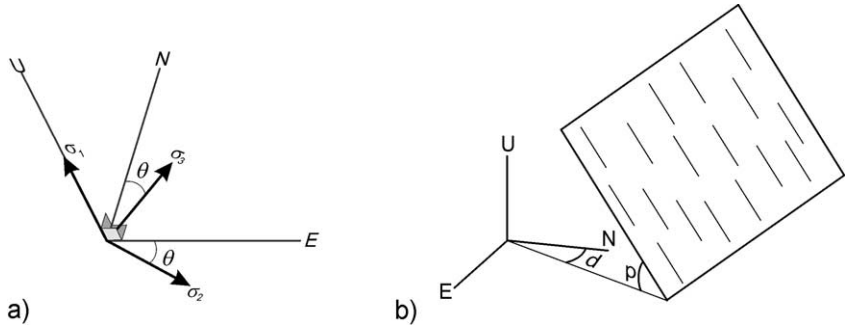

Fig. 11. Conventions adopted for calculations in Appendix A. (a) Applied stress state in 3DEC models, σ_1 is vertical and σ_3 is referenced by its strike θ. (b) Considered fault plane, its dip direction and dip are noted d and p, respectively. E = East, N = North, U = Up.

where

$$T = \begin{pmatrix} \sigma_1 & 0 & 0 \\ 0 & \sigma_2 & 0 \\ 0 & 0 & \sigma_3 \end{pmatrix} \tag{8}$$

is the stress tensor referenced to its principal axes, and

$$\mathbf{n} = \begin{pmatrix} \sin d \sin p \\ \cos d \sin p \\ \cos p \end{pmatrix} \tag{9}$$

is the unit vector normal to the fault plane and pointing upwards.

From Eqs. (6)–(9), it is easy to derive the following ones:

$$\sigma_n^2 = (\Delta\sigma)^2(\sin^2(d-\theta)\sin^2 p\Phi + \cos^2 p + \sigma_3/\Delta\sigma)^2, \tag{10}$$

$$\tau^2 = (\Delta\sigma)^2[\sin^2(d-\theta)\sin^2 p(1-\sin^2(d-\theta)\sin^2 p)\Phi^2 - 2\sin^2(d-\theta)\sin^2 p\cos^2 p\Phi + \cos^2 p(1-\cos^2 p)]^2, \tag{11}$$

where $\Delta\sigma = \sigma_1 - \sigma_3$ is the differential stress and $\Phi = (\sigma_2 - \sigma_3)/(\sigma_1 - \sigma_3)$ is the "shape ratio" (Angelier, 1975, 1994).

We introduce:

$$a = \sin^2(d-\theta)\sin^2 p, \tag{12}$$

$$b = \cos^2 p, \tag{13}$$

$$c = \sigma_3/(\sigma_1 - \sigma_3). \tag{14}$$

Eqs. (6) and (7) are rewritten as:

$$\sigma_n^2 = (\Delta\sigma)^2(a\Phi + b + c)^2, \tag{15}$$

$$\tau^2 = (\Delta\sigma)^2[a(1-a)\Phi^2 - 2ab\Phi + b(1-b)]^2. \tag{16}$$

Considering cohesionless faults, the Mohr–Coulomb (i.e. Eq. (4)) criterion is written as:

$$\tau^2 - (\mu\sigma_n)^2 \geq 0, \tag{17}$$

where μ is the coefficient of friction of the fault plane.

Combining Eqs. (15), (16) and (17), the criterion is given as a parabolic function of Φ:

$$A(d,p,\theta,\mu)\Phi^2 + B(d,p,\theta,\mu,\sigma_3/\Delta\sigma)\Phi + C(p,\mu,\sigma_3/\Delta\sigma) \geq 0, \tag{18}$$

with A, B and C equal to:

$$A = a(1 - a(1+\mu^2)), \tag{19}$$

$$B = -2a(b + \mu^2(b+c)), \tag{20}$$

$$C = b(1-b) - \mu^2(b+c)^2. \tag{21}$$

References

Angelier, J., 1975. Sur l'analyse de mesures recueillies dans des sites faillés: l'utilité d'une confrontation entre les méthodes dynamique et cinématique. C. R. Acad. Sci. Paris 281, 1805–1808 (erratum; ibid., 1976, 283, 466).

Angelier, J., 1994. Paleostress analysis of small-scale brittle structures. In: Hancock, P. (Ed.), Continental Deformation. Pergamon, Tarrytown, NY, pp. 53–100. Chapter 4.

Angelier, J., Colletta, B., Anderson, R.E., 1985. Neogene paleostress changes in the Basin and Range: a case study at Hoover Dam, Nevada-Arizona. Geol. Soc. Amer. Bull. 96, 347–361.

Barrier, E., Angelier, J., 1986. Active collision in Eastern Taïwan: the coastal range. Tectonophysics 125, 39–72.

Bergerat, F., 1987. Stress fields in the European platform at the time of Africa–Eurasia collision. Tectonics 6, 99–132.

Bott, M.H.P., 1959. The mechanics of oblique slip faulting. Geol. Mag. 96, 109–117.

Brown, E.T., Hoek, E., 1978. Trends in relationships between measured in-situ stresses and depth. Int. J. Rock Mech. Min. Sci. Geomech. Abstr. 15, 211–215.

Byerlee, J.D., 1978. Friction of rocks. Pure Appl. Geophys. 116, 615–626.

Carey, E., 1976. Analyse numérique d'un modèle mécanique élémantaire appliqué à l'étude d'une population de failles: calcul d'un tenseur moyen des contraintes à partir des stries de glissement. Thèse de troisième cycle, Tectonique Générale, Univ. Paris-Sud, Orsay, 138 pp.

Carey, E., Brunier, B., 1974. Analyse théorique et numérique d'un modèle mécanique élémentaire appliqué à l'étude d'une population de failles. C. R. Acad. Sci. Paris 279, 891–894.

Carmichael, R.S., 1989. Practical Handbook of Physical Properties of Rocks and Minerals. CRC Press, Boca Raton.

Cundall, P.A., 1971. A computer model for simulating progressive large scale movement in blocky rock systems. International Symposium on Rock Mechanics. International Society of Rock Mechanics, Nancy, p. II-8.

Cundall, P.A., 1980. UDEC, a generalised distinct element program for modelling jointed rock. U.S. Army European Research Office and Defence Nuclear Agency, Contract Report DAJA 37-39-C-0548.

Cundall, P.A., 1988. Formulation of a three dimensional distinct element model: Part I. A scheme to detect and represent contacts in a system composed of many polyhedral blocks. Int. J. Rock Mech. Min. Sci. Geomech. Abstr. 25, 107–116.

Dupin, J.-M., Sassi, W., Angelier, J., 1993. Homogeneous stress hypotheses and actual fault slip: a distinct element analysis. J. Struct. Geol. 15, 1033–1043.

Dupin, J.-M., Angelier, J., Sassi, W., 1994. L'hypothèse de jeux de failles indépendamment contrôlés par un état de contrainte unique est-elle valable? Une approche numérique 3D. Bull. Soc. Geol. Fr. 165, 317–328.

Gapais, D., Cobbold, P.R., Bourgeois, O., Rouby, D., de Urreiztieta, M., 2000. Tectonic significance of fault slip data. J. Struct. Geol. 22, 881–888.

Gephart, J.W., Forsyth, D.W., 1984. An improved method for determining the regional stress tensor using earthquake focal mechanism data: application to the San Fernando earthquake sequence. J. Geophys. Res. 89, 9305–9320.

Hancock, P.L., 1985. Brittle microtectonics: principles and practice. J. Struct. Geol. 7, 437–457.

Huchon, P., Jestin, F., Cantagrel, J.-M., Gaulier, J.M., Al Khirbash S., Gafaneh, A., 1991. Extensional deformations in Yemen since Oligocene and the Africa–Arabia–Somalia triple junction. Ann. Tecton. 2, 141–163.

Jaeger, J.C., Cook, N.G.W., 1979. Fundamentals of Rock Mechanics. Chapman & Hall, London, 515 pp.

Last, N.C., Harper, T.R., 1990. Response of fractured rock subject to fluid injection: Part I. Development of a numerical model. Tectonophysics 172, 1–31.

Le Pichon, X., Bergerat, F., Roulet, M.-J., 1988. Plate kinematics and tectonics leading to the Alpine belt formation: a new analysis. Processes in Continental Lithospheric Deformation. Spec. Pap. Geol. Soc. Am., vol. 218, pp. 111–131.

Letouzey, J., 1986. Cenozoic paleo-stress pattern in the Alpine foreland and structural interpretation in a platform basin. Tectonophysics 132, 215–231.

Maerten, L., 2000. Variations in slip on intersecting normal faults: implications for paleostress inversion. J. Geophys. Res. 270, 197–206.

Mattauer, M., Mercier, J.L., 1980. Microtectonique et grande tectonique. Mém. Hors-Sér. - Soc. Géol. Fr. 10, 141–161.

Mercier, J.L., Sorel, D., Simeakis, K., 1987. Changes in the state of stress in the overriding plate of a subduction zone: the Aegean Arc from the Pliocene to the Present. Ann. Tecton. 1 (1), 20–39.

Pascal, C., 1998. Etude mécanique et modélisation de la fracturation en extension, application au domaine de la Mer du Nord. Unpublished PhD thesis, Sciences de la Terre, Univ. P. and M. Curie, Paris, 410 pp.

Pascal, C., Gabrielsen, R.H., 2001. Numerical modelling of Cenozoic stress patterns in the Mid Norwegian Margin and the northern North Sea. Tectonics 20 (4), 585–599.

Petit, J.-P., 1987. Criteria for the sense of movement on fault surfaces in brittle rocks. J. Struct. Geol. 9, 597–608.

Pollard, D.D., Salitzer, S.D., Rubin, A.M., 1993. Stress inversion methods: are they based on faulty assumptions? J. Struct. Geol. 15, 1045–1054.

Ramberg, I.B., Gabrielsen, R.H., Larsen, B.T., Solli, A., 1977. Analysis of fracture pattern in Southern Norway. Geol. Mijnb. 56, 295–310.

Reches, Z., 1978. Analysis of faulting in three-dimensional strain field. Tectonophysics 47, 109–129.

Reches, Z., 1983. Faulting of rocks in three-dimensional strain fields: II. Theoretical analysis. Tectonophysics 95, 133–156.

Reches, Z., 1987. Determination of the tectonic stress tensor from slip along faults that obey the Coulomb yield condition. Tectonics 6, 849–861.

Reches, Z., Dieterich, J.H., 1983. Faulting of rocks in three-dimensional strain fields: I. Failure of rocks in polyaxial, servo-control experiments. Tectonophysics 95, 111–132.

Tibaldi, A., 1998. Effects of topography on surface fault geometry and kinematics: examples from the Alps, Italy and Tien Shan, Kazakstan. Geomorphology 24, 225–243.

Twiss, R.J., Geffel, M.J., 1990. Curved slickenfibers: a new brittle

sense indicator with application to a sheared serpentinite. J. Struct. Geol. 12, 471–481.
Twiss, R.J., Unruh, J.R., 1998. Analysis of fault slip inversions; do they constrain stress or strain rate? J. Geophys. Res. B 103 (6), 12205–12222.
Twiss, R.J., Protzman, G.M., Hurst, S.D., 1991. Theory of slickenline patterns based on the velocity gradient tensor and microrotation. Tectonophysics 186, 215–239.
Wallace, R.E., 1951. Geometry of shearing stress and relation to faulting. J. Geol. 59, 118–130.
Wallace, R.E., Morris, H.T., 1986. Characteristics of faults and shear zones in deep mines. Pure Appl. Geophys. 124, 107–125.
Zoback, M.-L., Anderson, R.E., Thompson, G.A., 1981. Cainozoic evolution of the state of stress and style of tectonism of the Basin and Range Province of the Western United States. In: Vine, F.J., Smith, A.G. (Eds.), Extensional Tectonics Associated with Convergent Plate Boundaries. Philos. Trans. R. Soc. Lond. Ser. A: Math. Phys. Sci., vol. 300. Royal Society of London, London, UK, p. 1454.